Regional Dynamics of Seasonal Variability in the South China Sea

ZHENGYU LIU AND HAIJUN YANG*

Department of Atmospheric and Oceanic Sciences, University of Wisconsin—Madison, Madison, Wisconsin

QINYU LIU

Institute of Physical Oceanography, The Ocean University of Qingdao, Qingdao, China

(Manuscript received 14 July 1999, in final form 17 April 2000)

ABSTRACT

Dynamics of the seasonal cycle of sea surface height (SSH) in the South China Sea (SCS) are studied using observations as well as numerical and theoretical models. Seasonal variability of the SCS is interpreted in light of large-scale dynamics and Rossby waves. It is found that the seasonal cycle over most of the SCS basin is determined predominantly by the regional ocean dynamics within the SCS. The SSH variability is shown to be forced mainly by surface wind curl on baroclinic Rossby waves. Annual baroclinic Rossby waves cross the basin in less than a few months, leaving the upper ocean in a quasi-steady Sverdrup balance. An anomalous cyclonic (anticyclonic) gyre is generated in winter (summer) by the anomalous cyclonic (anticyclonic) wind curl that is associated with the northeasterly (southwesterly) monsoon. In addition, surface heat flux acts to enhance the wind-generated variability. The winter surface cooling (warming) cools (warms) the mixed layer especially in the central SCS, reducing (increasing) the SSH.

1. Introduction

The South China Sea (SCS) has its main body of water contained in the central region (5°–23°N, 110°–120°E), and on average depth is over 2000 m (Fig. 1). One distinctive feature of the upper-ocean circulation within the SCS is a dramatic seasonal variability, suggested to be driven primarily by the South China Sea monsoon wind (Fig. 2, upper panels) (Wyrtki 1961). The circulation in the upper SCS has been studied using ship drift observations (Wyrtki 1961) and historical hydrographic data (e.g., Wrytki 1961; Guan 1978; Xu et al. 1980; Shaw 1989, 1991; Chu et al. 1997; Chu and Chang 1997; Chu et al. 1998b), and more recently with satellite altimetry (Shaw et al. 1999). These studies indicate that the basin-scale circulation of the upper SCS are generally cyclonic in the winter, reversing to largely anticyclonic in the summer. Major features of the seasonal variability in the SCS have been studied in numerical ocean models (Pohlmann 1987; Shaw and Chao 1994; Chao et al. 1996a, b; Metzger and Hurlburt 1996, 2001; Chu et al. 1998a). Nevertheless, a simple and unified dynamic frame work has yet to be fully developed. Furthermore, most of the previous studies have focused on the cases with an open boundary in the Luzon Strait; the role of the regional dynamics within the SCS has not been fully evaluated. The major objectives of this paper are twofold. First, we attempt to explore the extent to which the seasonal variability in the SCS can be explained by the dynamic processes locally within the SCS. Second, we attempt to present a simple dynamic frame work that can be applied to the seasonal sea surface height (SSH) variability in the SCS.

Altimeter observations from the TOPEX/Poseidon (T/P) mission (Chambers et al. 1997) and hydrography data will be used to provide a consistent picture of the seasonal circulation change in the upper layer of the SCS. These observations will be presented here mainly for comparison with model simulations. The driving mechanism for the seasonal variability of SSH in the SCS and the associated upper-ocean circulation will be investigated in terms of simple theoretical models, as well as an ocean general circulation model (OGCM). To focus on the regional dynamics within the SCS, we will focus our discussion on the results of models that have a closed Luzon Strait. The observed seasonal variability of SSH is shown to be well simulated by simple and complex ocean models over most of the basin. The

* Additional affiliation: Institute of Physical Oceanography, The Ocean University of Qingdao, Qingdao, China.

Corresponding author address: Z. Liu, 1225 W. Dayton St., Madison, WI 53706-1695.
E-mail: zliu3@facstaff.wisc.edu

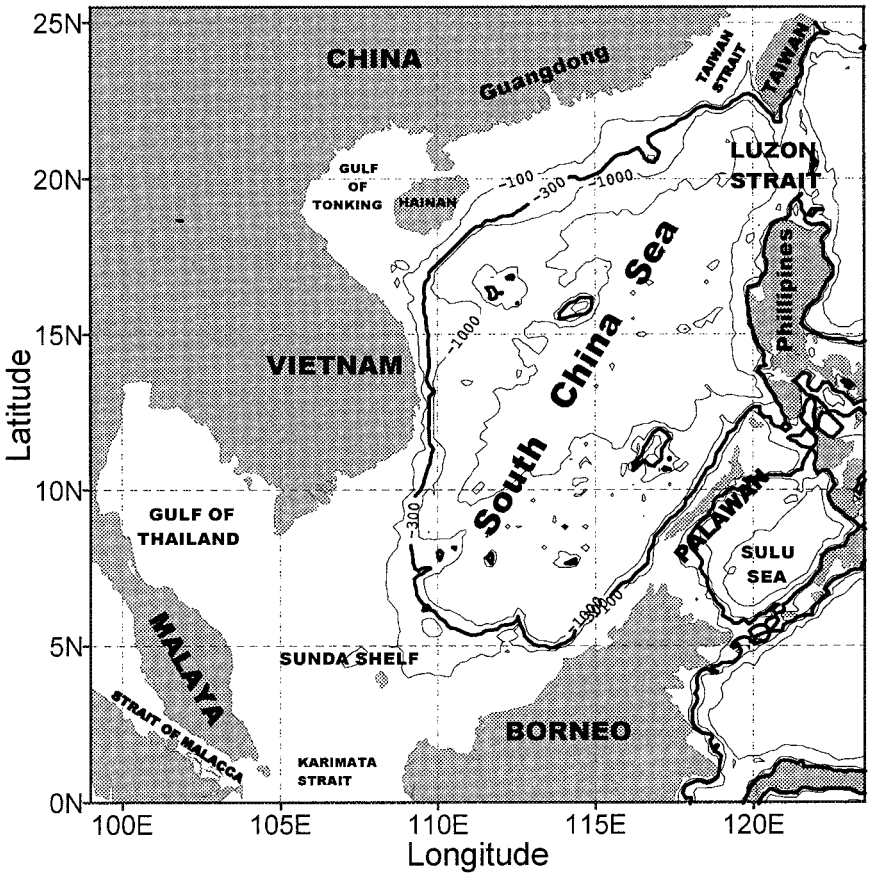

FIG. 1. Bathymetry of the South China Sea. The 300-m isobath, indicated by the heavy solid line, is used as the model domain for the planetary wave model (1) and the barotropic Sverdrup model (3) (islands are removed).

major seasonal flow in the upper layer of the SCS is shown to be forced dominantly by the wind curl on baroclinic planetary waves. The upper-ocean flow is, to a large extent, in the instantaneous Sverdrup balance because of the rapid transit of baroclinic planetary waves across the SCS. Surface heat flux also contributes significantly to the seasonal circulation change through its forcing of surface steric height. However, north of 19°N in the latitudes of Luzon Strait, SSH variability is poorly simulated for models with a closed boundary. Further experiments show that the Luzon Strait is important for the correct simulation of SSH variability in the most northern part of the SCS, confirming the results of some previous studies (Chu et al. 1998a). This paper is arranged as follows. In section 2, observational data and various numerical and theoretical models are described. Section 3 compares the SSH derived from observations and model simulations, and investigates the dynamic mechanisms of the seasonal variability. A summary and some discussions on the effect of open boundary will be presented in section 4.

2. Data, model, and theory

a. Data

Two datasets are used to extract basin-scale features of the seasonal cycle of the upper SCS. The first is Levitus climatological hydrography (Levitus and Bayer 1994a,b), which will be used to calculate dynamic sea level heights (η_{Levitus}). The other independent dataset is T/P altimetry data ($\eta_{\text{T/P}}$) (1992–98), which is composed into a seasonal climatology. The T/P data are corrected for all media and instrument effects (ionosphere, wet and dry troposphere, and electromagnetic bias) and geophysical effects (tides and inverted barometer) (Chambers et al. 1997). We use a gridded/smoothed version ($1° \times 1°$ resolution) compiled by the Center for Space Research, University of Texas (Chambers et al. 1997). The spatial filter used for the data is a rectangular Gaussian-squared filter spanning 1000 km in longitude and 400 km in latitude, with a roll-off of 400 km. The T/P SSH, with the nearest track 200 km away, may not capture small-scale features realistically; it should, how-

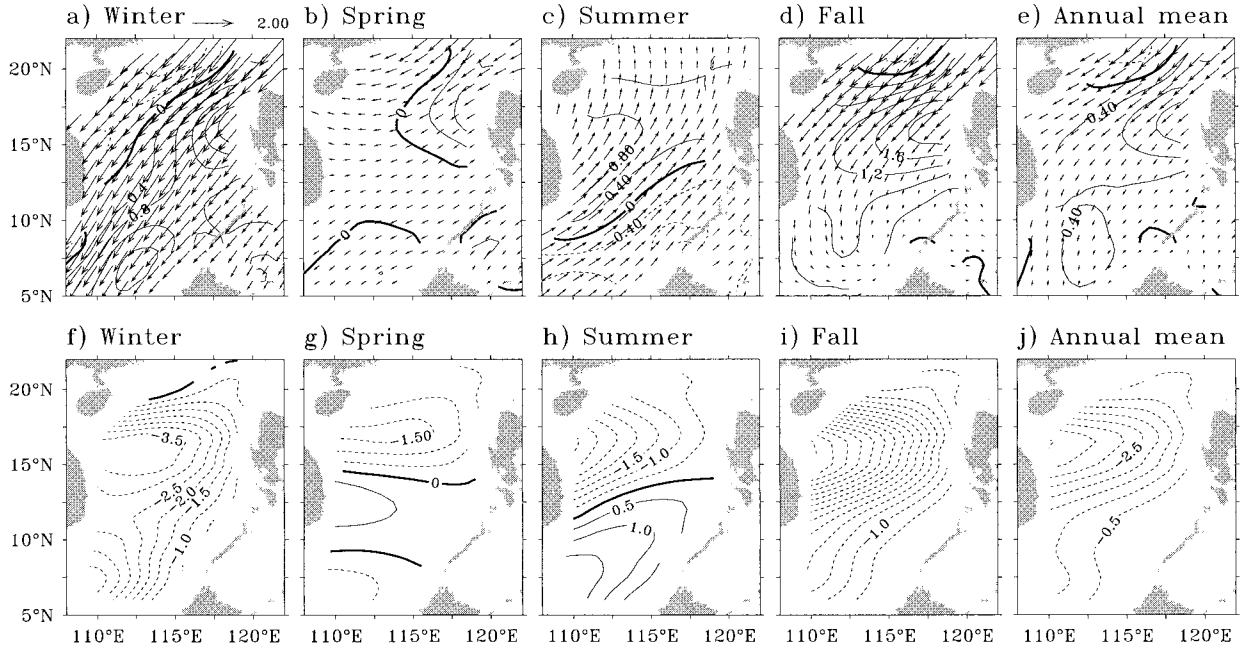

FIG. 2. (top) COADS wind stress τ/ρ_0 (vectors, 10^{-5} m^2 s^{-2}) and wind stress curl curl(τ/ρ_0) (CI: 0.4×10^{-10} m s^2) for (a) winter (Dec–Feb), (b) spring (Mar–May), (c) summer (Jun–Aug), (d) fall (Sep–Nov) and (e) annual mean. Negative wind stress curl is dashed. (bottom) Barotropic transport streamfunction Ψ for (f) winter, (g) spring, (h) summer, (i) fall, and (j) annual mean. Negative values are in dashed contours (CI: 0.5×10^6 m^3 s^{-1}).

ever, be reasonably adequate for basin-scale features in the SCS as shown recently by Shaw et al. (1999).

b. Model and theory

Three models will be applied to the SCS: two theoretical models and one OGCM. To focus on the regional dynamics within the SCS, the three models will have a closed Luzon Strait unless otherwise specified. The principle theoretical model is the 1.5-layer baroclinic planetary wave model, which will be used to simulate and understand the seasonal variability of the SCS upper-ocean circulation. The model equation can be written in terms of the perturbation thermocline depth h as

$$\partial_t h - C\partial_x h = -w_e. \tag{1}$$

Here, $x = a\cos\theta(\lambda - \lambda_0)$ is the distance in the zonal direction, with θ, λ, and a being the latitude, longitude, and the radius of the earth, respectively; $C = \beta L_D^2$ is the wave speed of the first baroclinic long Rossby wave; $L_D^2 = g'H/f^2$ is the baroclinic deformation radius, with $g' = g\Delta\rho/\rho_0$ being the reduced gravity and H the mean thermocline depth; $w_e = \text{curl}(\tau/\rho_0 f)$ is the Ekman pumping velocity. The mean stratification in the SCS gives approximately $H = 400$ m and $g' = 3$ cm s^{-2}, which correspond the planetary wave speed C of about 10 cm s^{-1} at 20°N and 40 cm s^{-1} at 10°N, respectively. The results presented are, however, not sensitive to these parameters, as long as the annual planetary wave is sufficiently fast.

The planetary wave model has been used frequently in the study of upper-ocean baroclinic variability, but mostly for large oceans (e.g., Kessler 1989; Jacobs et al. 1994; Sturges and Hong 1995). This model should also apply to the SCS. First, the spatial scale of the SCS is on the order of 1000 km, which is much larger than the baroclinic deformation radius (<100 km in the SCS). Consequently, relative vorticity is negligible. Second, although the SCS is a low-latitude sea, its major water body is located poleward of 5°N of the equator, so geostrophic balance should characterize the flow beneath the surface Ekman layer. Third, the vertical structure of the SCS has a strong thermocline (not shown), which can therefore be approximated by a 1.5-layer fluid.

The smallness of the SCS ocean basin, however, does make the annual variability in the SCS different from that in large oceans. With wave speeds of 40 cm s^{-1} to 10 cm s^{-1}, the planetary wave crosses the SCS (of about 1000 km) in 1 to 4 months. This short thermocline adjustment time implies that the local variability term in (1) is not dominant under an annual forcing. Instead, the forced planetary wave response (1) degenerates to a quasi-steady response $-C\partial_x h \approx -w_e$, which can be rewritten as

$$\beta H v_g \approx f w_e, \tag{2}$$

where the thermocline flow is $v_g = g'\partial_x h/f$. This will be called the *upper-ocean baroclinic* Sverdrup balance here.

The other theoretical model is the Sverdrup model (Pedlosky 1996)

$$\beta\partial_x\Psi = \text{curl}(\tau/\rho_0), \quad (3)$$

where Ψ is the total transport streamfunction for flows integrated in the entire water column. Equation (3), which here will be called *total* or *barotropic* Sverdrup balance to be distinguished from (2), can be shown valid for a flat bottom ocean after the rapid barotropic adjustment process, regardless of stratification. This model has recently been applied to the SCS (Shaw et al. 1999; Yang et al. 2000). Here, it is used as a reference, including the estimate of the anomalous barotropic dynamic height. As a crude approximation, a flat bottom, $D_0 = 2000$ m, is adopted here [realistic topographic cases are discussed in Yang (2000)]. The total Sverdrup balance (3) is similar to the upper ocean Sverdrup balance (2) because, outside the equatorial region where the Ekman transport is weaker than the Sverdrup transport, the strength of the wind curl is comparable to the Ekman pumping $\text{curl}(\tau/\rho_0) \sim fw_e$. Therefore, the barotropic transport Ψ and the upper ocean transport $g'Hh$ $(=H\int v_g\,dx)$ are comparable in magnitude and similar in spatial pattern.

The establishment of the upper-ocean Sverdrup flow (2) can be understood from the oceanic adjustment process (Anderson and Gill 1975). When a wind stress forcing is imposed over the SCS, barotropic Rossby waves rapidly cross the basin in several days, leaving a barotropic Sverdrup flow $v_B = \partial_x\Psi/D_0$ that has little vertical shear. Later after the first baroclinic wave crosses the basin in a month or so, the abyssal flow is diminished while the total transport still satisfies the total Sverdrup relation (3). Now, the flow is strongly baroclinic and the transport is concentrated only in the upper-ocean flow v_g. Consequently, the total Sverdrup relation (3) reduces to the upper-layer Sverdrup balance (2). Since the baroclinic flow v_g is stronger than the barotropic flow v_B by a factor of $v_g/v_B \sim D_0/H$, the baroclinic dynamic height

$$\eta_C = h\Delta\rho/\rho_0$$

is stronger than the barotropic dynamic height

$$\eta_B = \Psi f/gD_0$$

by a factor of

$$\eta_C/\eta_B \sim D_0/H. \quad (4)$$

For the SCS, the mean depth is about 400 m for the thermocline and 2000 m for the ocean bottom. Therefore, η_C is expected to be about five times larger than η_B.

In our simulation of the seasonal cycle of the SCS, both the planetary wave model (1) and the barotropic Sverdrup model (3) will be forced by the climatological Comprehensive Ocean Atmosphere Data Set (COADS) (da Silva et al. 1994) wind stress. The model domain is chosen along the 300-m isobath (Fig. 1). The models are solved with the characteristic method. The SSH [in (1)] and the streamfunction [in (3)] are assumed to be zero along the eastern boundary of the basin.

The three-dimensional Princeton Ocean Model (POM) (Blumberg and Mellor 1987) is used in conjunction with simple models to shed light on the driving mechanism of the seasonal cycle. We will discuss mainly a POM simulation of the SCS that has a closed boundary on the Luzon Strait and other straits. The model has 0.5° resolution, 24 sigma levels, and a realistic bottom topography. To examine the sensitivity of Luzon Strait, experiments are also carried out with a Pacific model domain, which will be discussed later in section 4. [For more details see Yang (2000).] For all the POM experiments, COADS climatological wind stress is applied; the surface heat flux is calculated as a restoring toward the climatological annual cycle of sea surface temperature (SST) with the restoring coefficient calculated from the COADS data; the surface salinity flux is calculated with the $E - P$ (evaporation minus precipitation) climatology from COADS. The POM is initialized with the annual mean Levitus temperature and salinity in the SCS. The model is run for ten years, of which the last five years of simulation are composed into a seasonal cycle. The POM has several particularly desirable features that are lacking in the simple models: it has more complete dynamics, such as boundary currents, mesoscale eddies, bottom topography, and nonlinearity; it includes the surface steric response to heat flux forcing, which usually accounts for a large part of the annual cycle of SSH in the extratropics; it also includes coastal upwelling process, which may be important for small oceans such as the SCS.

3. Seasonal cycle in the SCS

a. Wind forcing and Sverdrup flow

We first briefly describe the seasonal cycle of the monsoon wind, the wind stress curl, and the corresponding barotropic Sverdrup flow. Similar discussions have been carried out in recent work (Shaw et al. 1999; Yang et al. 2000). The surface wind stress over the SCS (Figs. 2a–e) reflects a strong northeasterly flow in winter (Fig. 2a); the winter monsoon retreats during spring, especially in the southern part (Fig. 2b); the summer southwesterly monsoon is established first in the southern and central part of the SCS, then expanding to the entire SCS (Fig. 2c); the summer monsoon is replaced by the northeasterly monsoon in fall, first from the northern SCS (Fig. 2d). Since the winter monsoon is much stronger than the summer monsoon, the annual mean wind (Fig. 2e) closely resembles the northeasterly wind in the fall (Fig. 2d).

The wind stress curl and the associated Sverdrup transport Ψ [see (3)] are presented in Figs. 2a–e (contours) and Figs. 2f–j, respectively. In winter, the Sverdrup flow exhibits a grand basinwide cyclonic gyre, that

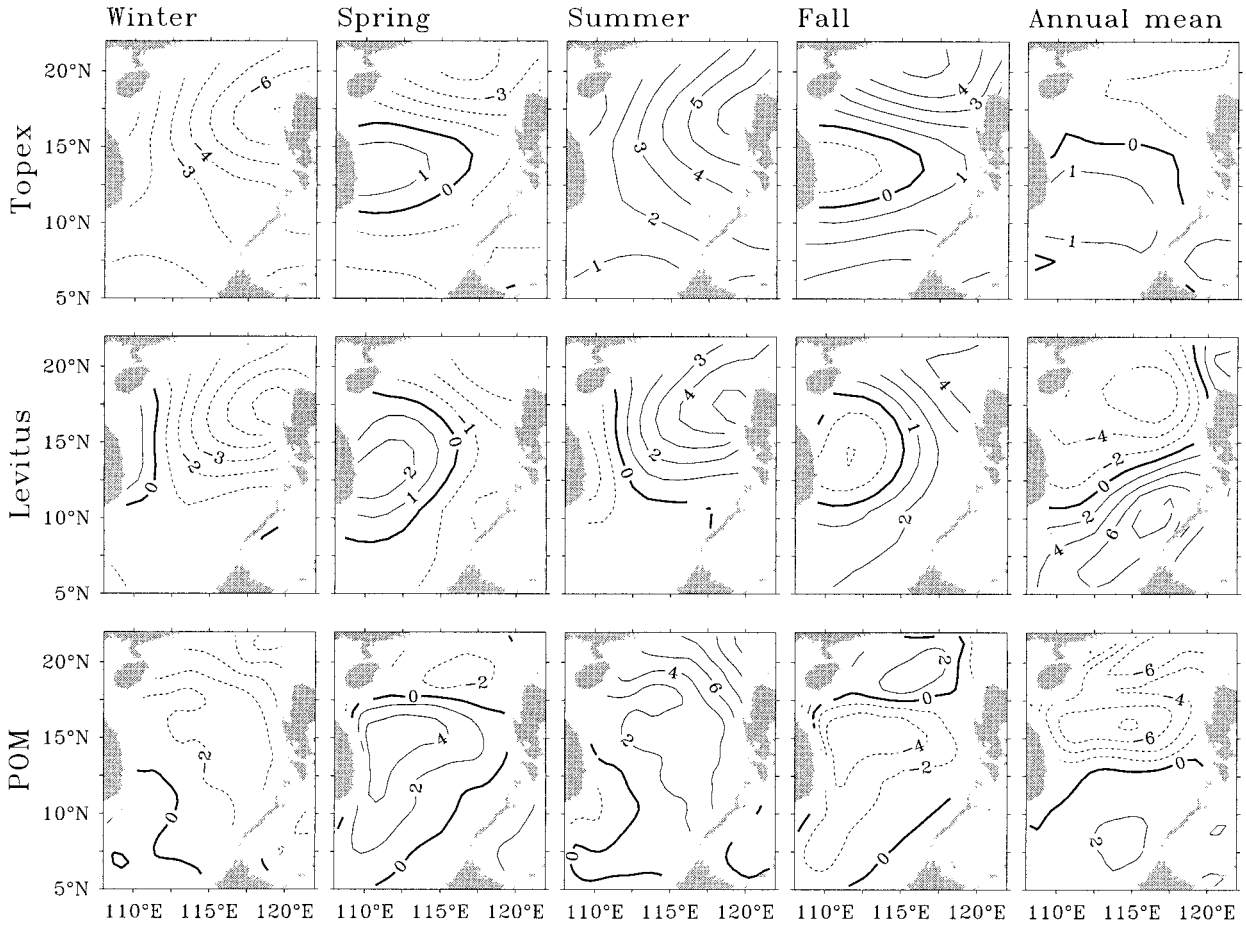

FIG. 3. SSH seasonal anomalies and annual mean (from top to bottom) for T/P altimetry $\eta_{T/P}$ (CI: 1 cm), Levitus total steric height $\eta_{Levitus}$ (CI: 1 cm), and POM SSH η_{POM} (CI: 2 cm). For the annual mean, a basinwide average is subtracted.

contains two subgyres: the northern SCS gyre and the southern SCS gyre, separated at about 13°N, each with a transport of about 4 Sv (Sv $\equiv 10^6$ m^3 s^{-1}) (Fig. 2f). These cyclonic gyres are forced by the cyclonic wind curl, principally generated by the cyclonic shear east of the northeasterly monsoon flow axis. The cyclonic wind curl has two maxima centered against the islands of the Phillipines and Borneo. These maxima are responsible for the northern and southern SCS gyres, respectively. Additionally, at the northern margin, anticyclonic wind shear forces a weak anticyclonic gyre (Fig. 2f). In spring, the cyclonic gyres weaken substantially (Fig. 2g) due to the diminishing winter monsoon. Because the winter monsoon decreases most dramatically in the southern part of the SCS, the cyclonic southern SCS gyre virtually disappears and, eventually in summer, is replaced by a modest anticyclonic southern SCS gyre that separates from the coast of Vietnam at 12°N (Fig. 2h). This anticyclonic gyre is forced by the anticyclonic wind shear of the southwesterly monsoon in the southern part of the SCS (Fig. 2c). The cyclonic northern SCS gyre, now forced by the southwesterly wind unlike in the winter, persists with modest strength. Unlike in the other seasons when the wind stress curl is dominated by shear, the summer cyclonic wind stress curl seems to be dominated by the curvature vorticity: the southwesterly flow changes direction from southwesterly to southerly as it proceeds from the southern to the northern SCS, generating cyclonic curvature vorticity (Fig. 2c). In fall, the monsoon reverses to northeasterly flow, especially in the northern SCS, reversing the basin circulation to cyclonic flow, with a maximum in the northern SCS (Fig. 2i). The annual mean Sverdrup flow is cyclonic (Fig. 2j), resembling the fall pattern (Fig. 2i).

The above discussion on the barotropic Sverdrup flow should be expected to directly apply to the upper-ocean flow. This is because we expect the upper ocean to nearly be in Sverdrup balance (2) at the annual period. This will be confirmed in the next section.

b. Seasonal cycle of SSH

Seasonal anomalies of SSH are plotted in Fig. 3 (left four columns) together with the annual mean field (right column). The SSH from the POM simulation (η_{POM}) is shown in the bottom row. The T/P SSH ($\eta_{T/P}$) is pre-

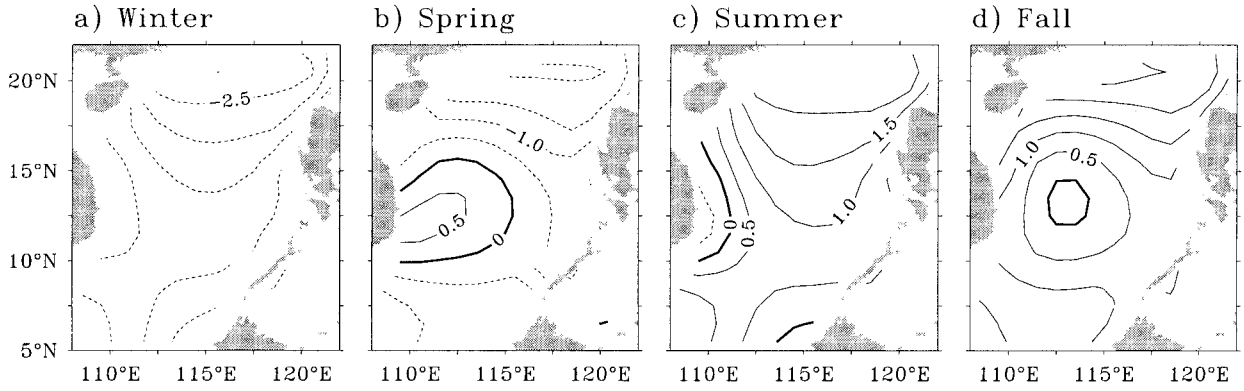

FIG. 4. Seasonal anomalies of surface steric height $\eta_{\text{Levitus50}}$ calculated from the Levitus temperature and salinity in the upper 50 m. (CI: 0.5 cm).

sented in the first row. The annual mean T/P altimetry data is included here, mainly for completeness, but should be regarded with great caution because of large geoid errors in the annual mean altimetry data (Wunsch and Stammer 1998). The second row presents the total steric height calculated using the Levitus data. The seasonal anomalies are calculated as

$$\eta_{\text{Levitus}}(x, y, t) = -\int_{-D}^{0} [\rho(x, y, z, t) - \rho_m(x, y, z)]\, dz/\rho_0,$$

while the annual mean is calculated as

$$\eta_{\text{Levitus}}(x, y) = -\int_{-D}^{0} [\rho_m(x, y, z) - \rho_M(z)]\, dz/\rho_0,$$

where D is the depth of the ocean, ρ_m is the annual mean density, and ρ_M is the horizontal average of ρ_m.

The seasonal anomalies of all three fields resemble each other (Fig. 3). The winter pattern (column 1) is dominated by a low (negative) SSH anomaly centered against the Philippines; the spring (column 2) is dominated by a high (positive) SSH anomaly centered against the coast of Vietnam, which appears to shift eastward toward the Philippines in summer (column 3); and, finally, in fall, the high SSH anomaly weakens while a low SSH anomaly emerges against the coast of Vietnam. The magnitudes of the seasonal SSH anomalies of the T/P altimetry data and the Levitus data are also comparable. Both are in the range of 5 cm, with negative and positive maxima achieved in winter and summer, respectively. The POM SSH anomaly, however, seems to have a large amplitude. This large POM variability, in part, is due to the fine resolution and small-scale variability in POM.

The similarity of $\eta_{\text{T/P}}$ and η_{Levitus} is consistent with the recent work of Shaw et al. (1999). The similarity suggests that the bottom pressure contribution to the SSH is not important for seasonal variability in the SCS. Indeed, the bottom pressure contribution to the SSH can be derived from $\eta_{\text{bottom}} = \eta_{\text{T/P}} - \eta_{\text{Levitus}}$, assuming both $\eta_{\text{T/P}}$ and η_{Levitus} are perfect (Gill and Niiler 1973). Since $\eta_{\text{T/P}}$ and η_{Levitus} are similar in both the pattern and magnitude, η is small.

Surface steric height anomalies reflect the expansion/contraction of the water column in the mixed layer in response to surface heat flux forcing, and seem to contribute somewhat to the similarity of T/P altimetry, Levitus dynamic height, and the POM SSH seasonal anomalies. Figure 4 plots the seasonal anomalies of surface steric height, which is calculated using the Levitus data for the upper 50 m as

$$\eta_{\text{Levitus50}}(x, y, t) = -\int_{-50\,\text{m}}^{0} [\rho(x, y, z, t) - \rho_m(x, y, z)]\, dz/\rho_0.$$

The $\eta_{\text{Levitus50}}$ (Fig. 4) has a magnitude of about 1–2 cm, which is about 20% of the total steric height anomaly (η_{Levitus}) in Fig. 3. It is interesting that $\eta_{\text{Levitus50}}$ anomalies have spatial patterns similar to those of η_{Levitus} (Fig. 3, second row). In both cases, a negative center of seasonal SSH anomaly extends southwestward from the northern SCS in winter; a warm pool emerges in the central SCS against the coast of Vietnam in spring; the SSH anomaly patterns in summer and fall are nearly the opposites of those in the winter and spring, respectively. The low SSH anomalies in winter and fall are due to the winter cooling, while the high SSH anomalies in spring and summer are caused by the summer heating. The surface steric height anomaly has the same spatial scale as the total steric height anomaly and, therefore, contributes directly to the pressure gradient and, in turn, the upper-ocean geostrophic flow. This implies that the seasonal surface heat flux is an important forcing mechanism of the seasonal circulation in the upper layer of the SCS. In comparison, in a major ocean, such as the extratropical Pacific Ocean, the surface steric height anomaly has a much larger spatial scale than that of the total steric height anomaly, and therefore contributes little to the pressure gradient and basin-scale circulation.

c. Seasonal cycle of the dynamic SSH

Now, we further examine the component of SSH that is caused by Ekman pumping forcing on the density field in the thermocline, which will be called the dynamic SSH here. The dynamic SSH can be approximated by subtracting the surface steric height from the total SSH (Gill and Niiler 1973). Since neither the baroclinic planetary wave model (1) nor the barotropic Sverdrup flow (3) responds to the surface heat flux forcing, they only produce the variability of the dynamic SSH and, therefore, should be compared with the corresponding dynamic SSH derived from observations and OGCM. The left four columns of Fig. 5 present seasonal anomalies (total minus the annual mean) of dynamic SSH for the T/P altimetry ($\eta_{\text{T/P}} - \eta_{\text{Levitus50}}$, row 1), Levitus steric height ($\eta_{\text{Levitus}} - \eta_{\text{Levitus50}}$, row 2), the POM ($\eta_{\text{POM}} - \eta_{\text{POM50}}$, row 3), baroclinic SSH from the planetary wave model (1) (η_C, row 4), and the barotropic SSH from the barotropic Sverdrup model (3) (η_B, row 5). The annual-mean dynamic SSH fields are also presented in the right column. For the T/P data, Levitus data, and POM simulation the dynamic SSH has a spatial distribution that is similar to the total SSH in Fig. 3, but with an amplitude reduction of about 20%, because the surface steric height anomaly has a similar pattern with an amplitude about 20% of the total SSH (Fig. 4).

It is seen from Fig. 5 that the major features of the spatial patterns agree among the dynamic SSHs in the central SCS. The dynamic SSH is dominated by a low that extends into the southern SCS in winter. In spring, this low is replaced by a strong high SSH centered against the coast of Vietnam at about 15°N. The high SSH anomaly lasts through the summer, with the center migrating eastward off the coast. Finally, in fall, the SSH anomaly switches back to a negative center against the coast of Vietnam. The summer and fall patterns are like the inverse of the winter and spring patterns. The baroclinic height (η_C) has an amplitude about 70% of those of T/P and Levitus data; therefore, accounting for most of the observed seasonal variability. Furthermore, baroclinic planetary waves cross the SCS in a few months; therefore, at the lowest order, the baroclinic fields are in quasi-steady baroclinic Sverdrup balance (2), which, as discussed before, is similar to the barotropic Sverdrup balance (3). Although the barotropic height (η_B) has a similar pattern to the rest, it has a much smaller amplitude. The small barotropic contribution to SSH is consistent with Eq. (4).

It is clear now that the observed seasonal cycle of dynamic SSH with its implied upper ocean circulation represents the response of baroclinic planetary waves to Ekman pumping [as in (1)], which can be understood from the seasonal evolution of the upper-ocean Sverdrup flow (2). Consequently, the negative SSH anomalies in winter and fall (Fig. 5) correspond to the seasonal anomaly cyclonic gyres forced by the northeasterly winter monsoon (Figs. 2f,h), while the positive SSH anomalies in spring and summer (Fig. 5) are associated with the seasonal anomaly anticyclonic circulation forced by the southwesterly summer monsoon (Figs. 2g,i).

Some observational features are not well simulated in the models. First, none of the models successfully simulates the variability north of 18°N. This probably results from closing Luzon Strait, which seems to strongly influence the SCS north of 18°N (Shaw 1989, 1991; Chu et al. 1998a; Metzger and Hurlburt 1996, 2001; also see discussion later in section 4). Second, both T/P altimetry and Levitus steric heights (Fig. 5) show maximum variability along the coasts of the Philippines and Vietnam with opposite signs in winter and summer. This near-coast variability is likely to be forced by alongshore winds through coastal upwelling process (Wrytki 1961; Shaw et al. 1996). In winter, the northeasterly wind generates westward surface Ekman drift, which induces downwelling warming, or high SSH anomalies, against Vietnam, while generating upwelling cooling, or low SSH anomalies, along the Philippines. The opposite occurs in summer. These coastal variability centers are absent in the two simple models because of the lack of a coastal upwelling process. In contrast, the POM succeeds in the simulation of the coastal variability centers (Fig. 5) because of its inclusion of a coastal upwelling process.

Correlation coefficients and the ratio of seasonal variance are also calculated between various SSH fields with the T/P SSH fields (not shown). Correlation calculations reinforce our discussion above. Overall, the total T/P SSH and total Levitus steric height is correlated well above 0.6 almost over the entire basin, and the ratio of variances is close to one, implying a similar magnitude of seasonal variability. The three model simulations correlate well with the T/P altimetry in the central latitudes (10°–18°N) of the SCS, with a correlation of 0.6 or higher. The POM variance is larger than the T/P data; the baroclinic SSH variance from the wave model is comparable with the T/P dynamic SSH, and the barotropic SSH variance is much weaker than the T/P SSH. Correlation of the two simple models with the observations decreases toward the northern and southern end of the SCS. The former seems to be related to the lack of a Luzon Strait, while the latter seems to indicate the limitations of the planetary wave model (1) and the Sverdrup flow model (3) near the equator. The POM simulation still exhibits a fairly good correlation with the observations even in part of the northern and southern regions of the SCS. This implies that the coastal upwelling effect, that is absent in the two simple models, contributes to part of the seasonal SSH variability in the northern and southern part of the SCS.

d. Zonal migration of SSH

We now examine the zonal migration of SSH anomalies, which should further shed light on the forcing mechanism of seasonal variability. Figure 6 plots the

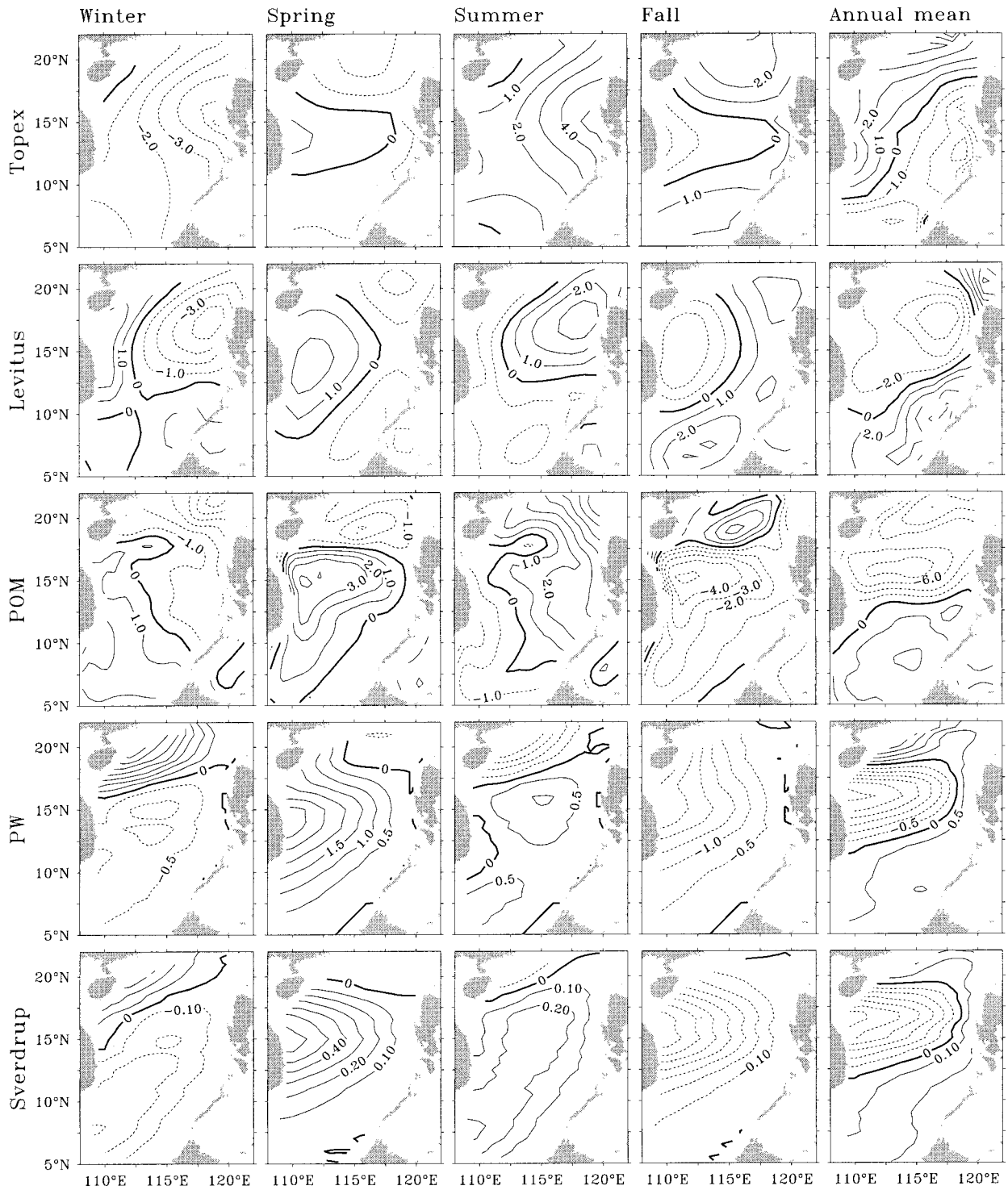

FIG. 5. Dynamic SSH seasonal anomalies (left 4 columns) and annual mean (right column). From top to bottom: T/P altimetry $\eta_{T/P} - \eta_{Levitus50}$ (CI: 1 cm), Levitus hydrography $\eta_{Levitus} - \eta_{Levitus50}$ (CI: 1 cm), POM SSH $\eta_{POM} - \eta_{POM50}$ (CI: 1 cm), baroclinic and barotropic dynamic SSHs η_C (CI: 0.5 cm), and η_B (CI: 0.1 cm) [defined before Eq. (4)]. Different from Fig. 3, a surface steric height anomaly is calculated in the upper 50 m using the Levitus data and is subtracted from the T/P altimetry and the Levitus steric height. A similar surface steric height anomaly is calculated from the POM model and is also subtracted from the POM SSH.

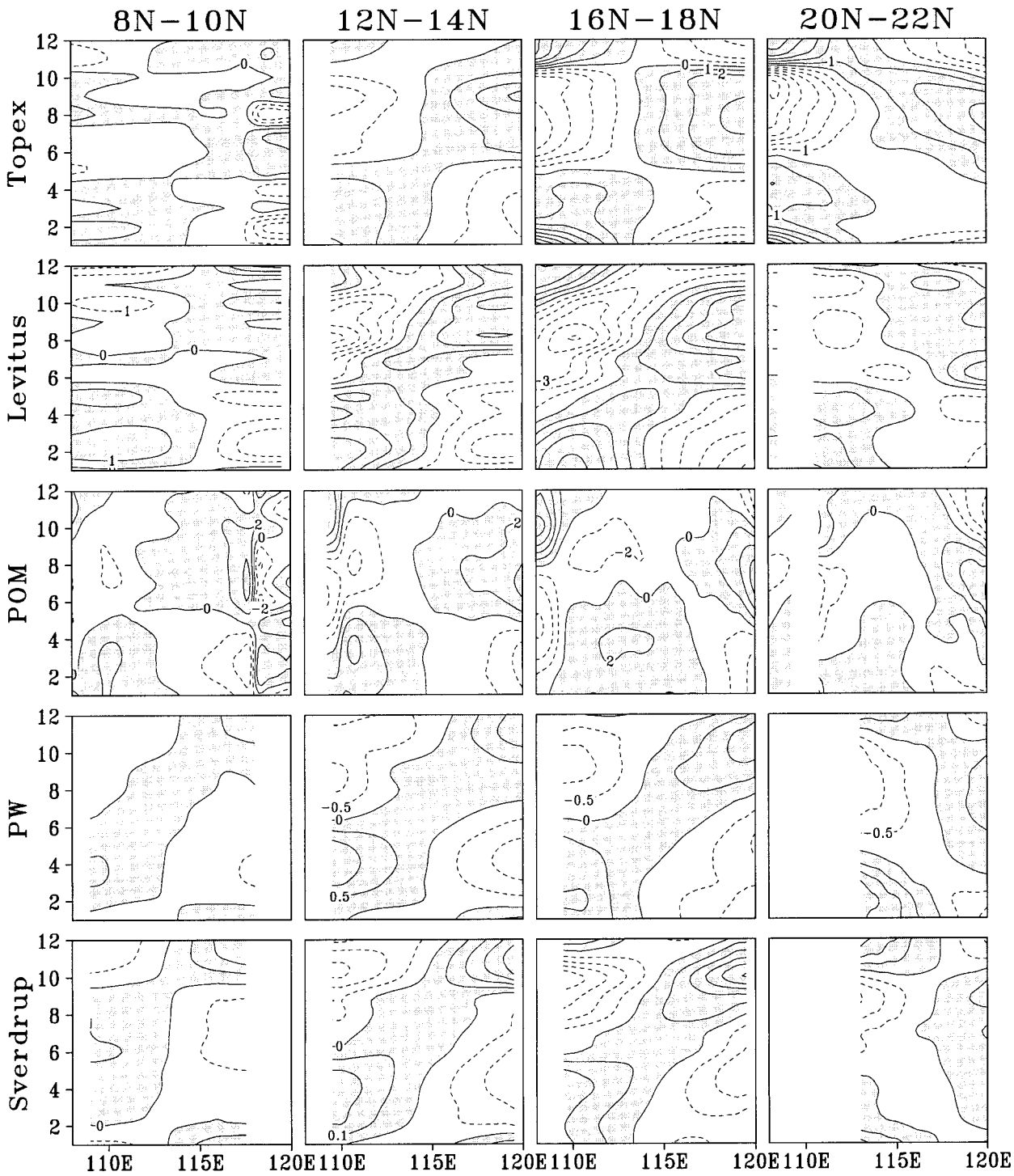

FIG. 6. Longitude–time plot of seasonal anomalies of SSH (zonal mean subtracted) in the latitude belts of (from left to right) 8°–10°N, 12°–14°N, 16°–18°N, and 20°–22°N. From top to bottom, the SSH anomalies are T/P altimetry ($\eta_{T/P}$), Levitus total steric height ($\eta_{Levitus}$), POM SSH (η_{POM}), the baroclinic dynamic height (η_C), and barotropic dynamic height (η_B).

time–longitude plot of $\eta_{T/P}$ (row 1), $\eta_{Levitus}$ (row 2), η_{POM} (row 3), η_C (row 4), and η_B (row 5) in the latitude belts 8°–10°N (column 1), 12°–14°N (column 2), 16°–18°N (column 3), and 20°–22°N (column 4). For each month, the zonal mean SSH has been subtracted. The zonal gradient of SSH and, in turn, the meridional geostrophic current of the upper ocean, therefore, remains undistorted throughout the seasonal cycle. Westward propagation of

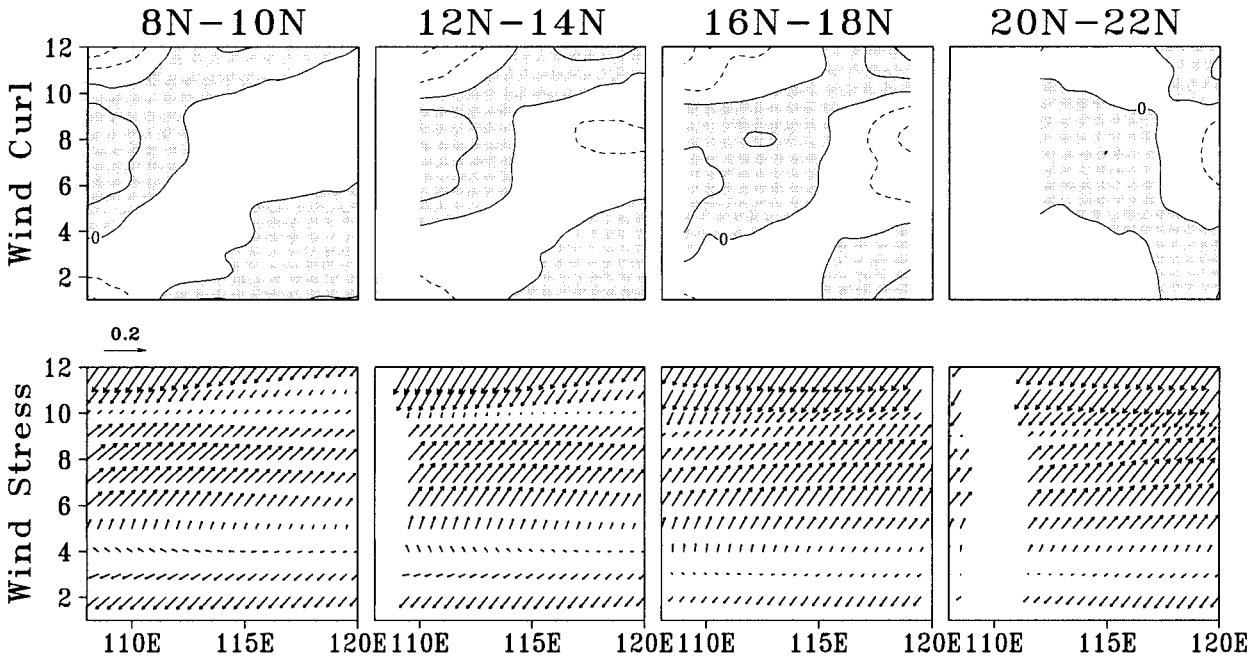

FIG. 7. Longitude–time plot of seasonal anomalies of wind stress curl (zonal mean subtracted) (top row) and wind stress vectors (bottom row) in the latitude belts of 8°–10°N (first column), 12°–14°N (second column) 16°–18°N (third column), 20°–22°N (right column).

planetary waves has been clearly identified in similar plots for large oceans (Jacobs et al. 1994; Chelton and Schlax 1996). Here, however, a weak westward propagation can be identified in observations (T/P SSH and Levitus steric height) only in the very northern latitude belt 20°–22°N. At other latitudes, surprisingly, the SSH anomaly clearly lacks a westward propagation. Indeed, the SSH anomaly seems to exhibit an eastward migration. Embedded in the zonal migration is a sudden change of SSH anomaly in winter and summer (particularly in the T/P altimetry), which seems to correspond to the sudden onset of the winter and summer monsoons. Furthermore, the high SSH that occurs in the western basin in winter is consistent with the broad southward geostrophic flow that forms part of the basin-scale cyclonic seasonal circulation anomaly (Fig. 5, column 1 of rows 1, 2), while the low SSH that emerges in the west during summer corresponds to the northward flow that forms part of the basinwide anticyclonic seasonal anomaly gyre in summer (Fig. 5, column 3 of rows 1, 2).

Except in the most northern latitude band (last column), major features of the zonal migration pattern are captured fairly well by the models, including the eastward migration apparent in the central latitudes and the sudden change of SSH anomaly in summer and winter. The westward migration of SSH in the most northern latitude band is, however, not well simulated; this seems to be related to the closed Luzon Strait. This similarity of zonal migration characteristics over most of the SCS is reflected in the correlation of results with the corresponding T/P altimetry anomalies. The correlation coefficients generally range from 0.5 to 0.8 (not shown).

It is conceivable that the zonal migration of SSH anomalies is caused mainly by the migration of the wind forcing, rather than the wave propagation. This speculation is confirmed by plotting the time–longtitude distribution for wind curl (Fig. 7, top row) and wind vectors (Fig. 7, bottom row). Except in the northernmost latitude belt, the wind switches from northeasterly to southwesterly in April and reversing back in November and the sudden change of wind stress can also be detected in the wind curl evolution. Embedded in the sudden change of monsoon wind, there is a weak tendency of eastward migration of wind curl. The westward integration of the wind curl anomaly, by which the Sverdrup transport (Fig. 6, bottom row) is calculated, enhances the appearance of eastward migration. Therefore, the zonal migration of SSH seasonal variability seems to be dominated by the wind-forced response, rather than free wave propagation. The dynamic cause of the zonal evolution of monsoon is beyond the scope of this work. We speculate that the wind curl evolution is related to the highly structured monsoon wind (Fig. 7, top row). This is in contrast to over large oceans, such as the Pacific, where the wind has a much larger spatial scale and, therefore, does not have such a highly structural wind curl anomaly, allowing the westward propagation of free planetary waves to be detected clearly (Jacobs et al. 1994; Chelton and Schlax 1996).

To examine the vertical structure of the migration, the total Levitus steric height is further decomposed into the contributions from four layers: 0–50 m represents the surface steric height anomaly in the mixed layer and is forced predominatly by the surface heat flux forcing; 50–100 m represents the upper thermocline and is forced mostly by the Ekman pumping; 100–500 m is

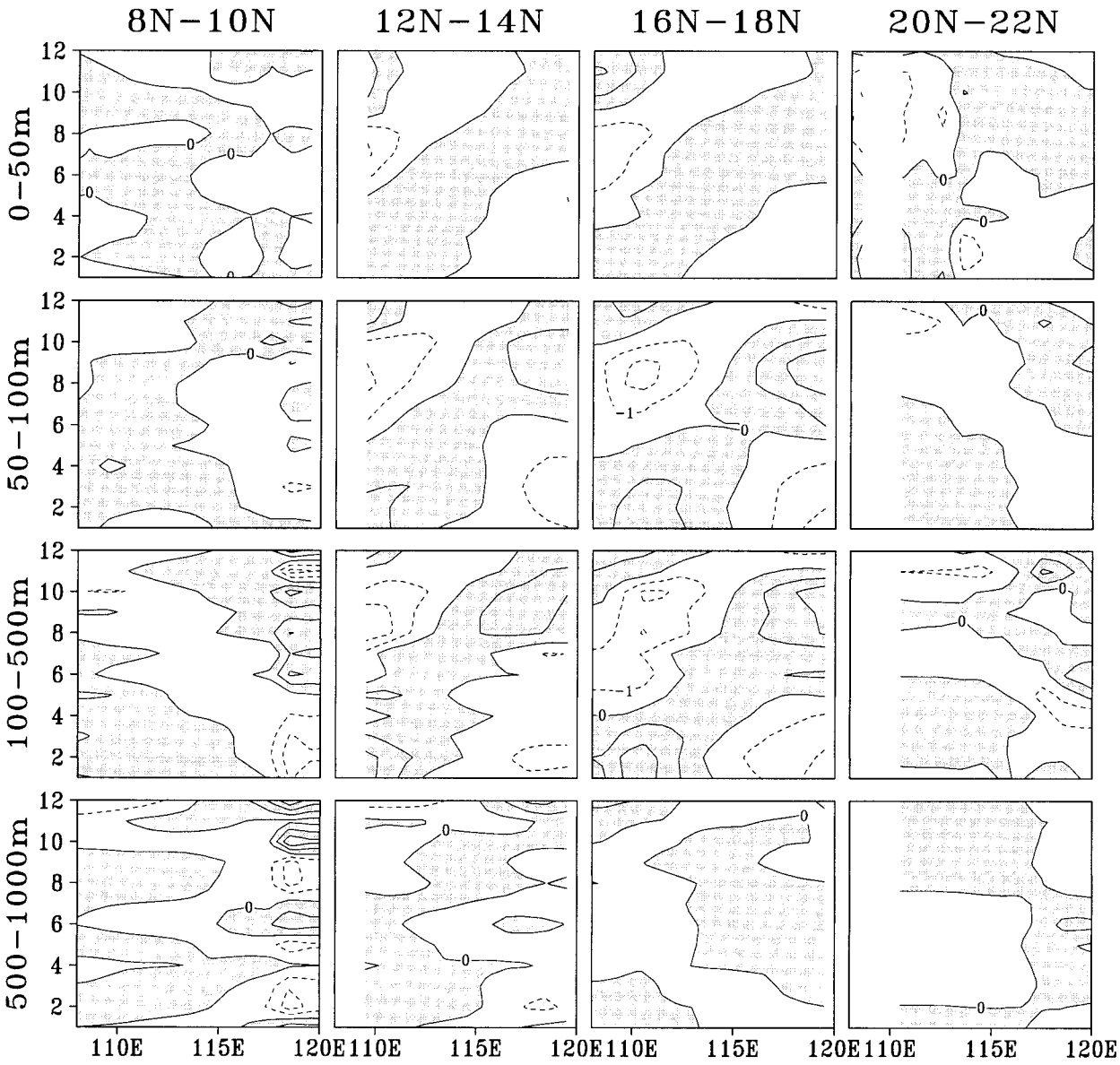

FIG. 8. Longitude–time plot of seasonal anomalies of steric height contribution (from top to bottom) 0–50 m, 50–100 m, 100–500 m, and 500–1000 m in the latitude belts of (left to right) 8°–10°N, 12°–14°N, 16°–18°N, and 20°–22°N. The sum of these four contributions equal the total Levitus steric height anomaly shown in the second row of Fig. 6.

the lower thermocline and is forced by the Ekman pumping; below 500 m represents intermediate water and abyssal water. Figure 8 shows the same time–longitude plot as in Fig. 6 but for the steric height contribution from the surface layer (0–50 m, row 1), the upper thermocline (50–100 m, row 2), the lower thermocline (100–500 m, row 3), and the deep ocean (500–1000 m, row 4). The correlations of the total steric height anomaly (Fig. 6, row 2) with the surface layer and upper and lower themocline layers are about 0.9, indicating a deep temperature perturbation that spans the entire thermocline (upper 500 m), or a first baroclinic mode response as assumed in the planetary wave model (1). The total steric height anomaly is composed mostly of thermocline variability, with the upper and lower thermocline contributing about equally. Therefore, as discussed before, Ekman pumping is the dominant forcing for the annual cycle. The surface steric height contributes about 20%, indicating the substantial role of the surface heat flux forcing.

4. Summary and discussions

The seasonal variability of SSH in the SCS is investigated with both observations and models. The SSH anomaly over most of the SCS appears to be forced

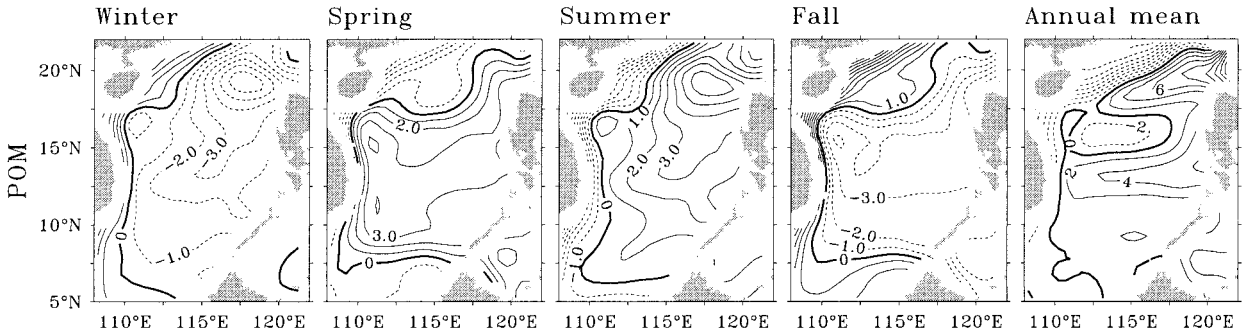

FIG. 9. Seasonal SSH anomalies as in Fig. 5 but for the Pacific domain POM simulation.

primarily by forcing within the SCS, first by surface dynamic forcing and secondarily by surface heat flux forcing. The shear of the northeasterly monsoon produces a strong cyclonic wind stress curl. The associated upward Ekman pumping forces an anomalous cyclonic gyre through a quasi-steady upper-ocean Sverdrup balance. In the mean time, winter cooling also lowers the SSH through the contraction of the surface water column. The opposite occurs in summer. The rapid translation of baroclinic Rossby waves across the SCS enables the seasonal variability to be determined by the baroclinic Sverdrup balance (2). The contribution of the barotropic Sverdrup flow (3) to the seasonal SSH, however, is negligible.

The much smaller amplitude of the SCS barotropic SSH, relative to the upper-ocean baroclinic SSH, is consistent with our estimates in Eq. (4). Gill and Niiler (1973) also pointed out that the baroclinic SSH is more important than the barotropic SSH south of 30°N in the North Pacific. The mechanism for the dominant baroclinic contribution in the SCS, however, is very different from the North Pacific. In the North Pacific, the baroclinic adjustment is much longer than a year; therefore, in (1) Ekman pumping is mainly balanced by local variability at the annual period. This balance results in a baroclinic SSH that is usually smaller than that from the baroclinic Sverdrup balance (2). Therefore, the ratio of the baroclinic to barotropic contributions is bounded by (4). The fast baroclinic adjustment time necessary for reaching this upper bound is most easily achieved in a small basin at low latitudes, such as the SCS. If the anomaly is narrowly confined near the surface layer, the contribution to the SSH anomaly from bottom pressure can be estimated to be comparable to that from the barotropic pressure. The small contribution of the barotropic component of SSH is also consistent with the small contribution of the bottom pressure, as implied by the similarity of the Levitus and T/P SSH anomalies (Fig. 5).

To demonstrate the role of Luzon Strait on the SCS, we present an experiment that has a model domain of the entire Pacific (north of 20°S). The experiments confirm previous studies that Luzon Strait has a significant influence on the SCS, especially in the northern part and along the western boundary region (Nitani 1972; Shaw 1989, 1991; Metzger and Hurlburt 1996, 2001; Chu et al. 1998a). Figure 9 plots the SSH seasonal anomalies as in Fig. 5 but for the Pacific domain POM simulation. The improvement in the region of northern SCS is evident. For example, in winter, the Pacific POM model produces a westward intrusion of Pacific water into the northern SCS, as indicated by the northward gradient of SSH anomalies in Luzon Strait. This winter intrusion of Pacific water has been observed (e.g., Shaw 1991) and can also be implied from the observed SSH anomaly (Fig. 5, top two rows), but it is not simulated in the closed boundary POM simulation (Fig. 5, row 3). The improvement in the region of northern SCS can also be seen in the enhanced correlation and variance as well as in the zonal migration (not shown). There is, however, no significant difference south of the latitudes of Luzon Strait in the interior SCS between the Pacific POM simulation (Fig. 9) and the closed boundary POM simulation (Fig. 5, row 3). This experiment substantiates our point that the SSH variability, except in the very northern part, is determined predominantly by local dynamics. It should be noticed that, as discussed before, part of the local dynamics is coastal upwelling, especially the strong upwelling along the coasts of the Philippines and Vietnam in winter and summer, respectively. Hence, the seasonal variability of SSH in the SCS is determined by three major elements: Rossby waves forced by wind stress curl, coastal upwelling, and the exchange flow through the Luzon Strait.

Acknowledgments. We thank Drs. Dongxiao Wang, J. Metzger, H. Hurlburt, P. Chu, and Mr. E. Bayler for helpful discussions. We also thank Dr. P. T. Shaw for bringing to our attention some recent relevant publications. Comments from two reviewers have helped to improve the manuscript. The altimetry data is downloaded from the Web page of the University of Texas, Center for Space Research. This work is supported by ONR, NSF, API/UW—Madison (ZL, HY), the Chinese NSF (HY, QL), and the Visiting Scholar Foundation of the Keylab at the University of Ministry of Education in China.

REFERENCES

Anderson, D., and A. Gill, 1975: Spin-up of a stratified ocean with applications to upwelling. *Deep-Sea Res.,* **22,** 583–596.

Blumberg, A. F., and G. L. Mellor, 1987: A description of a three-dimensional coastal ocean circulation model. *Three Dimensional Coastal Ocean Models*, N. S. Heaps, Ed., Amer. Geophys. Union, 1–16.

Chambers, D., B. Tapley, and R. Stewart, 1997: Long-period ocean heat storage rates and basin-scale heat fluxes from TOPEX. *J. Geophys. Res.,* **102,** 10 525–10 533.

Chao, S. Y., P. T. Shaw, and S. S. Wu, 1996a: Deep water ventilation in the South China Sea. *Deep-Sea Res.,* **43,** 445–466.

——, ——, and ——, 1996b: El Niño modulation of the South China Sea circulation. *Progress in Oceanography,* Vol. 38, Pergamon, 51–93.

Chelton, D. B., and M. G. Schlax, 1996: Global observations of oceanic Rossby waves. *Science,* **272,** 234–238.

Chu, P. C., and C. P. Chang, 1997: South China Sea warm pool in boreal spring. *Adv. Atmos. Sci.,* **14,** 195–206.

——, S. Lu, and Y. Chen, 1997: Temporal and spatial variability of the South China Sea surface temperature anomaly. *J. Geophys. Res.,* **102,** 20 937–20 955.

——, Y. Chen, and S. Lu, 1998a: Wind-driven South China Sea deep basin warm-core/cool-core eddies. *J. Oceanogr.,* **54,** 347–360.

——, C. Fan, G. Lozano, and J. Kerling, 1998b: An airborne expendable bathythermograph survey of the South China Sea, May 1995. *J. Geophys. Res.,* **103,** 21 637–21 652.

da Silva, A., C. Young, and S. Levitus, 1994: *Atlas of Surface Marine Data 1994.* Vol. 1: *Algorithms and Procedures.* NOAA Atlas NESDIS 6.

Gill, A., and P. Niiler, 1973: The theory of the seasonal variability in the ocean. *Deep-Sea Res.,* **20,** 141–177.

Guan, W. X., 1978: The South China Sea warm current—A winter counter-wind current outside Quangdong coastal ocean (in Chinese). *Oceanol. Limonol.,* **9,** 117–127.

Jacobs, G. A., H. E. Hurlburt, J. C. Kindle, E. J. Metzger, J. L. Mitchell, W. J. Teague, and A. G. Wallcraft, 1994: Decade-scale trans-Pacific propagation and warming effects of an El Niño anomaly. *Nature,* **370,** 360–363.

Kessler, W., 1989: Observations of long Rossby waves in the northern tropical Pacific. NOAA Tech. Memo. ERL PMEL-86, 169 pp.

Levitus, S., and T. P. Bayer, 1994a: *World Ocean Atlas.* Vol 3: *Salinity,* NOAA Atlas, NESDIS, U.S. Dept. Commerce, 99 pp.

——, and ——, 1994b: *World Ocean Atlas.* Vol. 4: *Temperature,* NOAA Atlas, NESDIS, U.S. Dept. Commerce, 117 pp.

Metzger, E. J., and H. E. Hurlburt, 1996: Coupled dynamics of the South China Sea, the Sulu Sea, and the Pacific Ocean. *J. Geophys. Res.,* **101** (C5), 12 331–12 352

——, and ——, 2001: The nondeterministic nature of Kuroshio penetration and eddy shedding in the South China Sea. *J. Phys. Oceanogr.,* in press.

Nitani, H., 1972: Beginning of the Kuroshio. *Kuroshio,* H. Stommel and K. Yoshida, Eds., University of Washington Press, 129–163.

Pedlosky, J., 1996: *Ocean Circulation Theory.* Springer-Verlag, 453 pp.

Pohlmann, T., 1987: A three dimensional circulation model of the South China Sea. *Three-Dimensional Models of Marine and Estuarine Dynamics,* J. C. J. Nihoul and B. M. Jamart, Eds., Elsevier, 245–268.

Shaw, P. T., 1989: The intrusion of water masses into the sea southwest of Taiwan. *J. Geophys. Res.,* **94,** 18 213–18 226.

——, 1991: The seasonal variation of the intrusion of the Philippine Sea water into the South China Sea. *J. Geophys. Res.,* **96,** 821–827.

——, and S. Y. Chao, 1994: Surface circulation in the South China Sea. *Deep-Sea Res. I,* **41,** 1663–1683.

——, ——, K. K. Liu, S. C. Pai, and C. T. Liu, 1996: Winter upwelling off Luzon in the northeastern South China Sea. *J. Geophys. Res.,* **101,** 16 435–16 448.

——, ——, and L. Fu, 1999: Sea surface height variations in the South China Sea from satellite altimetry. *Oceanol. Acta,* **22,** 1–17.

Sturges, W., and B. G. Hong, 1995: Wind forcing of the Atlantic thermocline along 32°N at low frequencies. *J. Phys. Oceanogr.,* **25,** 1706–1714.

Wunsch, C., and D. Stammer, 1998: Satellite altimetry, the marine geoid, and the oceanic general circulation. *Annu. Rev. Earth Planet. Sci.,* **26,** 219–253.

Wyrtki, K., 1961: Physical oceanography of the Southeast Asian waters. *Scientific Results of Marine Investigations of the South China Sea and the Gulf of Thailand,* Vol. 2. NAGA Report, Scripps Institution of Oceanography, 195 pp.

Xu, X., Z. Qiu, and H. Cheng, 1980: A survey of the circulation of the SCS (in Chinese). *Proc. Chinese Oceanography and Limonology Conf. on Hydrological Meteorology,* 137–145.

Yang, H., 2000: Simulation of the circulation of the South China Sea Ph.D dissertation, The Ocean University of Qingdao, 77 pp.

——, Q. Liu, and Z. Liu, 2000: The basin scale characteristics of seasonal variation of the Sverdrup circulation in the South China Sea (in Chinese). *Prog. Nat. Sci.,* in press.